Supporting Information for

Decoding a percolation phase transition of water at ~330K with a nanoparticle ruler

Carlos D. S. Brites[1†], Bilin Zhuang[2,3†], Mengistie L. Debasu[1,4], Ding Ding[5], Xian Qin[6], Fernando E. Maturi[1], Winnie W. Y. Lim[2], De Wen Soh[2], J. Rocha[4], Zhigao Yi[6], Xiaogang Liu[6,7*] and Luís D. Carlos[1*]*

[1]*Department of Physics and CICECO – Aveiro Institute of Materials, Universidade de Aveiro, 3810–193 Aveiro, Portugal.* [2]*Institute of High Performance Computing, Singapore 138632, Singapore.* [3]*Yale-NUS College, Singapore 138527, Singapore.* [4]*Department of Chemistry and CICECO – Aveiro Institute of Materials, Universidade de Aveiro, 3810–193 Aveiro, Portugal.* [5]*Institute of Materials Research and Engineering, Singapore 138634, Singapore.* [6]*Department of Chemistry, National University of Singapore, 117543, Singapore.* [7]*Joint School of National University of Singapore and Tianjin University, International Campus of Tianjin University, Fuzhou 350207, P. R. China.*

*e-mail: zhuangbl@ihpc.a-star.edu.sg, chmlx@nus.edu.sg, lcarlos@ua.pt
[†]These authors contributed equally to this work.

This PDF file includes:

> Materials and Methods
>
> Supplementary Text
>
> Supplementary Figs. S1 to S20
>
> Supplementary Tables S1 to S6
>
> References

Table of contents

S1 Materials and Methods

S1.1 Synthesis and characterization

Synthesis

Materials. Yttrium(III) acetate hydrate (99.9%), ytterbium(III) acetate hydrate (99.9%), erbium(III) acetate hydrate (99.9%), lutetium(III) acetate hydrate (99.9%), sodium hydroxide (> 98%), ammonium fluoride (> 98%), 1-octadecene (90%), and oleic acid (90%) were all purchased from Sigma-Aldrich and used as received unless otherwise noted.

Synthesis of NaYF$_4$:Yb/Er(18/2%)@NaYF$_4$ core-shell nanoparticles (24 nm)

The synthesis procedure was reported previously in Ref. 1.

Synthesis of ligand-free NaYF$_4$:Yb/Er(18/2%)@NaYF$_4$ core-shell nanoparticles. Ligand-free nanoparticles were obtained by a modified literature procedure[1]. Typically, the oleic acid-capped core-shell nanoparticles were dispersed in a solution containing ethanol (1 mL) and hydrochloric acid (1 mL; 1 M) and ultrasonicated to remove the oleic acid. The resulting ligand-free nanoparticles were collected by centrifugation at 16,500 rpm for 20 min, washed with ethanol and redispersed in deionized water (pH = 4.60$\pm$0.01).

Synthesis of ligand-free NaYF$_4$:Lu/Yb/Er (50/18/2%) nanoparticles (106 nm)

The fabrication of ligand-free NaYF$_4$:Lu/Yb/Er nanoparticles followed the same procedure adopted for the NaYF$_4$:Yb/Er@NaYF$_4$ core-shell nanoparticles. In a typical procedure, 2 mL aqueous solution of Ln(CH$_3$CO$_2$)$_3$ (0.2 M, Ln = Lu, Y, Yb, and Er) was added to a 50 mL flask containing 3 mL of oleic acid and 7 mL of 1-octadecene. The mixture was heated to 150 ºC for 1 h. After cooling down to 50 ºC, a methanol solution (6 mL) containing NH$_4$F (1.6 mmol) and NaOH (1 mmol) was added under stirring for 30 min. After removal of methanol by evaporation, the solution was heated to 290 ºC under argon for 3 h and then cooled down to room temperature. The resulting nanoparticles were washed with ethanol several times and re-dispersed in 4mL of cyclohexane.

Preparation of luminescent nanofluids. NaYF$_4$:Yb/Er@NaYF$_4$ core-shell nanoparticles (24 nm) were dispersed in water, cyclohexene, and toluene, whereas NaYF$_4$:Lu/Yb/Er nanoparticles (106 nm) were dispersed in water according to a literature procedure[1] (Table S1).

Materials characterization

Electron microscopy. Transmission electron microscopy (TEM, Figure S2a,b) measurements were carried out on a JEOL-JEM 2100F field-emission transmission electron microscope operated at an acceleration voltage of 200 kV.

pH measurements. The pH of the suspensions was measured with a portable pH meter (pH 330i, WTW, Germany) coupled to a combination electrode (Sentek, UK). Two-Point calibration of the pH meter was made using two buffer solutions with pH=4.0 and 7.0 (Sigma Aldrich). Aqueous suspensions of $NaYF_4$:Yb/Er@$NaYF_4$ and $NaYF_4$:Lu/Yb/Er nanoparticles (0.30 mL, 25 mg/mL) were separately dispersed in distilled water (1.70 mL, pH=5.40±0.01) and the pH of the suspensions were measured as 5.10±0.01 and 5.20±0.01, respectively. The pH of the suspension containing $NaYF_4$:Lu/Yb/Er nanoparticles was further changed using HCl (0.5 M) and NaOH (0.5 M) aqueous solutions. First, the pH of distilled water (4 mL) was adjusted to 2.60 using a few drops of the HCl solution. Then, an aqueous suspension of the nanoparticles (0.30 mL, 25 mg/mL) was dispersed in the above solution (1.70 mL) under sonication, and the final pH of the suspension is 2.70±0.01. Nanoparticles' aqueous suspensions with pH = 6.30±0.01 and 8.50±0.01 were prepared by adding drops of the NaOH solution to the distilled water. The mass of the nanoparticles in each suspension was 3.75 mg/mL, and the volume fraction was unchanged. The pH measurements were carried out at 20 °C for all luminescent nanofluids.

Dynamic light scattering and Zeta potential. Dynamic light scattering (DLS) and zeta potential (Figure S2c-f) measurements were carried out at 298 K using a Malvern Zetasizer Nano series instrument, Nano-ZS (Red badge operating with a 632.8 nm laser, Model ZEN3600, UK). A folded capillary cell (Malvern instruments, DTS1070) was used for both the DLS and Zeta potential measurements. For each point, three measurements with ten scans were carried out, and their average values were reported. For each point, three measurements with ten scans were carried out, and their average values were reported. The pH-dependent zeta-potential results shown in Figure **S7** indicate a stable colloidal system in almost all the studied range ($|\zeta|$≥25 mV)[2]. Moreover, the pH dependence is similar to that reported before for Er^{3+}/Yb^{3+} codoped $NaYF_4$ nanoparticles (mean particle size of ~25 nm)[3].

S1.2 Experimental setup for temperature measurements

The schematic experimental setup was presented in Figure S1. The scanning position of a CW infrared laser diode (980 nm) was controlled by a moving stage with a minimum step of 0.001 mm. In our study, a ThorLabs quartz cuvette (CV10Q1400) was used as the container and filled with 0.50 mL of a nanofluid. Table S1 summarizes the mass concentration and volume fraction of the different nanofluids used in this work. The temperature is increased at one side of the cuvette by thermal contact with a Kapton thermofoil heater (Minco) mounted in a Cu holder and coupled to a temperature controller (IES-RD31). The temperature controller is equipped with a Barnant thermocouple 100 (model 600-2820, sensitivity 0.1 K). The maximum heat flux from the Kapton thermofoil heater is computed by measuring the variation in the temperature of the Cu holder. Note that the heat capacity of the holder, C_h, is calculated as $C_h = m_h C_c = 8.1 \ \text{J} \cdot \text{K}^{-1}$, where m_h=21×10^{-3} kg is the mass of the holder and c_c=386 J·kg^{-1}·K^{-1} is the specific heat of Cu. Using the temperature increase rate $\Delta T/\Delta t$ for the temperature increments of 10 and 15 K, 0.16 and 0.24 K·s^{-1}, respectively (measured by the holder-embedded Barnant thermocouple), the corresponding heating power values $P = C_h \Delta T/\Delta t$ are 1.30 and 1.95 W, respectively. Taking the ratio of the heating power to the cuvette's contact area (28 mm^2), the maximum heat flow transferred to the nanofluid suspension Q is 4.63×10^4 and 6.95×10^4 W·m^{-2} for temperature increments of 10 and 15 K, respectively.

The detection system consists of a collimating lens (74-UV, Ocean Optics) and a USB-portable spectrometer (Maya 2000 Pro, Ocean Optics), connected by a QP450-1-XSR optical fiber (Ocean Optics). The spectrometer is controlled by a homemade MatLab® graphical user interface to real-time acquisition and pre-processing of the emission spectra with controllable integration window and boxcar. The baseline of the emission spectra of the luminescent nanofluids was removed, and the integrated areas of the Er^{3+} $^2H_{11/2} \rightarrow ^4I_{15/2}$ (I_H, 510–535 nm) and $^4S_{3/2} \rightarrow ^4I_{15/2}$ (I_S, 535–565 nm) transitions were computed. The thermometric parameter Δ is computed for each recorded emission spectrum using the I_H and I_S integrated areas. In all dynamic temperature measurements, the boxcar is maintained constant at one pixel (0.5 nm) and the integration time is set to 0.250 s.

S1.3 Thermometer calibration, relative thermal sensitivity and temperature uncertainty

The reduced temperature $\theta(t)$ is computed by:

$$\theta(t) = \frac{T(t) - T_i}{T_{max} - T_i} \tag{S1}$$

where $T(t)$, T_i and T_{max} are the instantaneous, initial and maximum temperature, respectively. Notice that $T(t)$ is determined through Eq. 3 of the manuscript.

The relative thermal sensitivity (S_r) is written as:

$$S_r = \frac{1}{\Delta}\left|\frac{\partial\Delta}{\partial T}\right| \tag{S2}$$

and the temperature uncertainty (δT) as:

$$\delta T = \frac{1}{S_r}\frac{\delta I}{I} \tag{S3}$$

The corresponding maximum relative thermal sensitivity and minimum temperature uncertainty are 1.13 ± 0.02 %·K^{-1} and 0.1 K (NaYF$_4$:Yb/Er@NaYF$_4$) and 1.12 ± 0.02 %·K^{-1} and 0.1 K (NaYF$_4$:Lu/Yb/Er).

S1.4 Signal denoising using the DWT method and critical onset time determination

We adopt a nonlinear noise reduction method, presented by Lang *et al.*[4], that uses the discrete wavelet transforms (DWT) that significantly improve the noise reduction, compared to the original wavelet-based approach[5, 6]. The intensity ratio denoising was implemented using a MatLab® routine that *i)* imports the as-measured intensity ratio, *ii)* converts the intensity ratio into temperature using Eq. S1, *iii)* calculates the reduced temperature using Eq. S2, *iv)* applies the DWT denoising procedure to generate a denoised reduced temperature (threshold parameter: 15, 5 stages) and *v)* computes the noise as the difference between the measured and the denoised reduced temperature. The histogram of the noise values was computed for all the denoised curves, following invariantly a Gaussian profile ($r^2 > 0.980$) centered at zero. Figure S8 shows an illustrative example. We conclude that the noise corresponds to an additive white Gaussian signal, thus validating the use of the DWT denoising procedure[5, 6].

The denoised intensity ratio was used to compute the critical onset time (t_{0i}). The routine marks t_{0i} as the time instant in which the denoised signal change is higher than the standard deviation of the noise (extracted from the histograms of the noise values).

S1.5 The crossover temperature

The crossover temperature, T_c, corresponds to the temperature of the intersection of the two straight lines representing the temperature dependence of the instantaneous ballistic Brownian velocity of the 24 and 106 nm upconverting nanoparticles between 300 to 355 K. A MatLab routine was designed to calculate all the possible combinations of two straight lines that fit the bilinear pattern in the mentioned temperature range, and to determine the best fit maximizing the product of the squared correlation coefficients of each line. The uncertainty, ΔT_c, is given by:

$$\Delta T_c = \frac{\sigma_e}{s} \tag{S4}$$

where σ_e and s are the standard error of the estimate and the slope of the linear regime for $T > T_c$, respectively, being the estimate calculated through:

$$\sigma_e^h = \sqrt{\frac{\sum (v - v')^2}{N - 2}} \tag{S5}$$

where v and v' are the measured and the fitted values of the Brownian velocity, respectively, and N is the number of data points for $T > T_c$. A scheme illustrating the determination of $T_c \pm \Delta T_c$ is presented in Figure S9.

S1.6 Temperature dependence of the instantaneous Brownian velocity of the nanocrystals

We repeated the procedure to determine the instantaneous Brownian velocity of the nanocrystals in several heating/cooling cycles generated in different days using distinct heat flows transferred to the nanofluid suspension ($Q = 4.63 \times 10^4$ and $Q = 6.95 \times 10^4$ W·m⁻²), observing systematically the same velocity values. The instantaneous Brownian velocity of the 24 nm nanoparticles in water (pH = 5.10±0.01) measured during three consecutive heating cycles between 303 and 343 K at $Q = 6.95 \times 10^4$ W·m⁻² is shown in Figure S10.

S1.7 Modeling the thermal transport

Brites *et al.*[1] demonstrated that the experimentally measured temperature onset does not obey a semi-infinite conduction model. As the experiment involves thermal excitation and measures a macroscopic temperature rise of the nanofluids, it is of interest to further

examine the heat transport physics of the experiment. First, we point out that convection in steady-state thermal measurements of fluids leads to the agreement with Newton's law of cooling[1]. However, the semi-infinite model based purely on conduction agrees well with the equivalent natural convection models[7] at the initial stage of the transport. Thus, we can assume the use of a pure conduction model is valid in determining the onset time in Figure S3 and Figure S4.

Here, we use a double parallel plate conduction model[8] to mimic the heat transport in our nanofluids experiment. As shown in Figure S15, the model assumes two infinitely large parallel plates separated by $L = 1$ cm (same as in the experiment). One plate is held at a temperature $T_h = T_L + \Delta T$ (where ΔT = 9, 21, and 25 K) and the other plate is held at T_L. The liquid is assumed to be pure water at the temperature T_L for the initial condition at $t = 0$. The solution to the one-dimensional heat conduction with the two-plate boundary condition and constant T_L under initial condition is[8]:

$$
T(x,t) = T_L + (T_h - T_L)\frac{x}{L} + \frac{2}{\pi}\sum_{n=1}^{\infty}\frac{T_h\cos n\pi - T_L}{n}\sin\frac{n\pi x}{L}\,e^{-\frac{\alpha n^2 \pi^2 t}{L^2}}
$$
$$
+ 2\,T_L\sum_{n=1}^{\infty}\sin\frac{n\pi x}{L}\,e^{-\frac{\alpha n^2 \pi^2 t}{L^2}}\frac{1-\cos n\pi}{n\pi}
$$

(S6)

Figure S16a-c, show examples of temperature rise at $x = 0.2$ cm for ΔT=9 K. For a different temperature gradient $T_h - T_L$ across the two plates, ΔT = 21 K (Figure S17a-c) and ΔT = 25 K (Figure S18a-c), $T(x,t)$ reaches a different temperature after 100 seconds. However, the maximum of the second-order derivative of Eq.S6 as a function of time occurs at the same position for all three $T_h - T_L$ values. We have used, thus, the maximum of the second-order derivative as the criterion to determine the onset time t_{0i} for each x_i position Figure S16b. Figure S17b and Figure S18b show the normalized temperature versus time and position using Eq.S6, mimicking Figure S3a-d and Figure S4a,b. The onset position versus time follows a linear trend. There are differences between the figures because Eq. S6 does not necessarily have the same boundary and initial conditions of the experiment. For instance, there is still a finite rise time of the water temperature at x=0, but this is not the case in the model. As already mentioned, this model does not consider the presence of convective effects, but the short time behaviour is almost the same with and without convection. In the Supplementary Information of Brites *et al.*[1], a one-dimensional conduction model is used

and a linear trend of position versus time cannot be obtained. Furthermore, the instantaneous velocity is independent of the temperature gradient $T_h - T_L$ across the entire cuvette. Figure S16a-c shows a temperature rise for three different values of $T_h - T_L$ (inducing a different final equilibrium temperature). However, the second-order derivative maximum is independent of $T_h - T_L$. This maximum recorded for each position x_i follows an approximately linear trend in Figure S16c, Figure S17c, and Figure S18c and a linear fit yields the instantaneous velocity. This velocity describes the motion of the interface between the hot and cold regions, where mixing due to the Brownian motion of the nanoparticles[1] occurs in the nanofluid.

A linear relationship is obtained between the instantaneous velocity of the nanoparticles v versus the thermal diffusivity of pure water α over the temperature range 0-100 °C, as shown in Figure S16d, Figure S17d, and Figure S18d. The data for the thermal diffusivity of pure water is derived from Refs. [9-11]. This linear relationship allows us to write $v = m\,\alpha$, where $m = 1.61$ m^{-1} and, the intercept is zero. There is no difference between the values of m obtained from the linear fit in Figure S16d, Figure S17d, and Figure S18d. With this linear relation, effective thermal diffusivity of the nanoparticle-water mixture can be obtained through linear interpolation, and the data for the enhancement factor compared to pure water (see Figure 2d of the manuscript).

S1.8 Molecular dynamics simulation of SWM4-NDP water model

We carry out molecular dynamics simulations for the polarizable SWM4-NDP water model[12] using an extended Lagrangian dynamics with a dual-Langevin thermostat[13] with the OpenMM package[14]. At each temperature, the size of the cubic simulation box is set such that the density of water molecules in the simulation box matches the density of water at atmospheric pressure (Table S5), with periodic boundary condition applied to the simulation box. For the dual-Langevin thermostat, the friction coefficients for the center-of-mass and for the internal Drude-pair degrees of freedom are 20 ps^{-1} and 1 ps^{-1}, respectively, and the temperature set for the internal Drude-pair is 1 K. The time step for the integration is 1 fs. For each randomly generated initial configuration, the system is first annealed from 373.15 K to the desired temperature in 100 equal-interval temperature steps and 1 ps per step, followed by equilibration at the desired temperature for 1 ns. Then, the configuration state of the water is sampled every 10 ps for 70 ns. The sampling is repeated independently for 8 times for each system size (512 molecules, 768 molecules, and 1024 molecules) and temperature (5 K intervals from 303.15 K to 363.15 K). Thus, for each system size, a total

of 56000 configuration states are sampled. Molecular dynamics simulation results shown in the main text are based on the system with 1024 molecules, and the effects of the finite size of the simulation results are shown in Figure S20 and Figure S21.

S1.9 Computation of orientational order parameters q and q_5

We hereby provide a rigorous mathematical definition for the orientational order parameters q and q_5 in Eqs. (1) and (2) in the main text. For a water molecule in consideration, let indices i=1 to 5 denote the first to the fifth nearest neighbor, where the distance between any two water molecules is the distance between the centers of their oxygen atoms. Let us define a function $Q_{i,j,k,l}$ for the water molecule to be:

$$Q_{i,j,k,l} = 1 - \frac{3}{8}\left[\left(\cos\psi_{ij} + \frac{1}{3}\right)^2 + \left(\cos\psi_{ik} + \frac{1}{3}\right)^2 + \left(\cos\psi_{il} + \frac{1}{3}\right)^2 + \left(\cos\psi_{jk} + \frac{1}{3}\right)^2 \right.$$
$$\left. + \left(\cos\psi_{jl} + \frac{1}{3}\right)^2 + \left(\cos\psi_{kl} + \frac{1}{3}\right)^2 \right]$$

(S7)

where $\psi_{\alpha\beta}$ denotes the angle extended from the oxygen atom of the molecule considered to the oxygen atoms of αth and β^{th} neighbors. It is easy to see that the definition of the orientational parameter q is simply:

$$q = Q_{1,2,3,4}$$

(S8)

Similarly, the orientational parameter q_5 in Eq. (2) in the main text can be equivalently written as:

$$q_5 = \max(Q_{1,2,3,4}, Q_{1,2,3,5}, Q_{1,2,4,5}, Q_{1,3,4,5}, Q_{2,3,4,5})$$

(S9)

S1.10 Peak maxima r_1 and r_2 of O-O pair distribution function

The O-O pair distribution function $g(r)$ is calculated with the Python *mdtraj* package[15], with a bin width of 0.005 Å. The pair distribution function at various temperature is plotted in Figure S19a, for the simulation with 1024 water molecules. The peak maxima of r_1 and r_2 are obtained by the least-squares fitting to a Gaussian function $a\ exp\left[-\left(\frac{x-b}{c}\right)^2 + d\right]$, where *a, b, c, and d* are fitting parameters, to the sampled $g(r)$ in the ranges 2.75 Å<r_1< 2.78 Å and 4.1 Å<r_2<4.9 Å, respectively. The Gaussian fitted curves are shown in Figure S19b and

Figure S19c. The peak maxima are given by the value of *b* in each fit. The use of Gaussian function in the fitting is the same as the procedure in Skinner *et al.*[16].

The bilinear trend in r_2 revealed by our simulation has not been observed in the simulations of Skinner *et al.*[16]. We note that the use of the nonpolarizable TIP4P/2005 model in their simulations might have overestimated the hydrogen-bond strength at higher temperatures. Here, we employ a polarizable model that captures more realistically the temperature dependence of the hydrogen-bond network[17].

S1.10 Molecular dynamics simulation using TIP4P-FB water model

To show that features observed in our simulation are not specific to the model chosen, we carried out molecular dynamics simulations for the nonpolarizable TIP4P-FB water model [18] using an extended Lagrangian dynamics with a Langevin thermostat with the OpenMM package[14]. At each temperature, the size of the cubic simulation box is set such that the density of water molecules in the simulation box matches the density of water at atmospheric pressure (Table S5). For the Langevin thermostat, the friction coefficients for the center-of-mass is 20 ps^{-1}. The time step for the integration is 1 fs. For each randomly generated initial configuration, the system is first annealed from 373.15 K to the desired temperature in 100 equal-interval temperature steps and 1 ps per step, followed by equilibration at the desired temperature for 1 ns. Then, the configuration state of the water is sampled every 10 ps for 9 ns. The sample size is 1024 molecules at temperatures 303.15 K, 333.15 K, 363.15 K. The simulation results are shown in Figure S21 and Figure S22.

S2 Supplementary Text

S2.1 Estimation of the probability of finding a cooperative region around the nanoparticle

In this section, we estimate the extensiveness of the hydrogen bond network based on the decomposition of molecules into the two local configuration states. For every molecule in each configuration state from the MD simulations, the molecule can be classified into the TH-state of the DT-state by comparing its values of *q* and q_5.

Then, we identify connected clusters of TH-state molecules linked in a hydrogen-bonding network in a low-density-liquid (LDL) motif. Two molecules are connected in the same LDL motif if both are in TH-state, and one is among the four nearest neighbors of the other. For water at ambient conditions, the individual hydrogen bonds may instantaneously break or

form due to thermal fluctuations. Despite this, the long-ranged tetrahedral network may survive at a longer timescale because the hydrogen bonds in a large network do not all break down simultaneously. In addition, through sampling with molecular dynamics simulations, we have also taken into account thermal fluctuations at the individual molecule level within the network.

An LDL motif connecting the left and the right border, the top and the bottom border, and the front and the back border is called a spanning cluster (under periodic boundary condition, as in our simulation, the boundary points need to be neighbors as well to form a spanning cluster). For each configuration state, we determine whether a spanning LDL motif is found. Our definition of a spanning cluster is stricter than the percolated cluster studied in most literature of percolation transition. Usually, a percolated cluster is defined as one that connects the left and the right border, the top and the bottom border, or the front and the back border, i.e., only one of the dimensions needs to be connected. However, in our work, since we are interested in motifs that span in all three dimensions, we require a spanning cluster to be connecting the borders in all three dimensions.

Based on the configuration states sampled from the molecular dynamics simulations at any particular temperature, we can compute $p_{span(simulation\ box)}$, the probability of finding a spanning cluster in the simulation box, being the fraction of instances where the configuration state has a spanning cluster.

To estimate the probability of finding an LDL cluster that spans a bigger volume, let us first consider a $n \times n \times n$ cubic array of simulation boxes. If an LDL cluster is to span the whole volume, then each of the simulation boxes in the cubic array has to be spanned by the cluster. This occurs with probability given by

$$p_{span} \approx \left(p_{span(simulation\ box)}\right)^{n \times n \times n} \tag{S10}$$

For a general cubic region with length $L \gg L_{simulation\ box}$, where $L_{simulation\ box}$ is the side length of the simulation box, the probability of finding a spanning LDL cluster can be obtained from a generalization of Eq. S10 as

$$p_{span}(V) \approx \left(p_{span(simulation\ box)}\right)^{\left(\frac{L}{L_{simulation\ box}}\right)^3} \tag{S11}$$

Applying Eq. S11 to the volume of the nanoparticles $L = d$, where d is the diameter of the nanoparticles, we can estimate the probability p_{span} of finding an LDL cluster spanning the size of the nanoparticles. The result for 24 nm nanoparticles is plotted in Figure 3D of the main text. However, to accurately estimate the p_{span} for a 106 nm nanoparticle, a higher accuracy for $p_{span(simulation\ box)}$ is needed, and that requires at least 10^6 configuration states sampled for simulations with 1024 water molecules. The 106 nm nanoparticle has a volume of 40,000 times of the simulation box with 1024 water molecules. If we are to have 25 independent samples for each of the 40,000 simulation boxes, this tallies to 10^6 configuration states. This is well beyond the computation power available for the current study.

S2.2 The effective mass

In this section, we consider the effective mass of the nanoparticles by analyzing the transport of the liquid in the immediate vicinity of the nanoparticles. In particular, we consider both the fluid that moves with the nanoparticle cooperatively.

First, to understand the hydrodynamic regime of the nanoparticle movement, we compute the Schmidt number $Sc = v/D$ of the nanofluid, where v is the kinematic viscosity of the fluid and D is the diffusion coefficient of the nanoparticle. The diffusion coefficient can be further estimated from the Stokes-Einstein-Sutherland formula $D = k_B T/6\pi\eta a$, where η is the dynamical viscosity of the fluid and a is the radius of the nanoparticle. For the nanofluids studied in this work, $Sc \sim 10^4 - 10^5$ is much greater than unity. Since $Sc \gg 1$, the nanoparticle is in the regime where the momentum transfer is more significant than mass diffusion[19]. In this regime of Brownian transport, a vortex shell of thickness d develops around the particle in Brownian motion[19].

Using a heuristic argument in the spirit to that discussed in Ref. 16, we may relate the effective mass to the nanoparticle mass and the mass of surrounding fluids. We let m_0 be the sum of the mass of the nanoparticle and of the fluid with which it moves cooperatively. At time-scales shorter than the momentum transfer (nanoconvection time scale, approximately 10^{-12} s)[1], the average speed is $v_0 = \sqrt{k_B T/m_0}$, given by the equipartition theorem. This speed is slowed down by hydrodynamic interactions with the fluid. At the time scale τ at which the energy of the Brownian motion propagates, the speed is determined by the conservation of momentum:

$$v = \frac{m_0\, v_0}{(m_0 + m_v)} \tag{S12}$$

where m_v is the mass of the vortex shell developed during time τ. Combining Eq. S12 and the equipartition theorem, we have:

$$v^2 = \frac{m_0 k_B T}{(m_0 + m_v)^2} = \frac{k_B T}{m^*} \tag{S13}$$

with the effective mass of the system given by $m^* = (m_0 + m_v)^2/m_0$.

For $T>T_C$, as the nanoparticle is not surrounded by the extended hydrogen network of the LDL motif, we may set m_0 to the mass of the bare nanoparticle. Given the radius of the nanoparticle a, the masses m_0 and m_v are $\frac{4}{3}\pi\rho_N a^3$ and $\frac{4}{3}\pi\rho_w[(a+d)^3 - a^3]$, respectively, where ρ_N and ρ_w are respectively the densities of the nanoparticle and the water. From the slope of the v^2 vs. T plot for $T>T_C$, we may estimate the thickness of the vortex shell from Eq. S13. The slopes for the 24 nm nanoparticle at pH=5.10 and for the 106 nm nanoparticle at pH=5.20 in water (Table S4) give a thickness of the vortex shell of about $d = 1 \times 10^{-7}$ m.

As the kinematic viscosity does not change drastically from $T>T_C$ to $T<T_C$, we may assume that the thicknesses of the vortex shell are the same in the whole temperature range concerned because of $d \sim \sqrt{\nu\tau}$.

At $T<T_C$, and since the nanoparticle is immersed within an extended hydrogen-bond network, there is a non-negligible mass of fluid moving cooperatively with the nanoparticle. In other words, the mass and the size of the nanoparticle are enlarged. Assuming the thickness of the cooperatively-moving fluid b, the mass m_0 should now include this fluid, that is $m_0 = \frac{4}{3}\pi\rho_N a^3 + \frac{4}{3}\pi\rho_w[(a+b)^3 - a^3]$. The mass of the vortex shell generated outside the cooperatively-moving fluid is $m_v = \frac{4}{3}\pi\rho_w[(a+b+d)^3 - (a+b)^3]$. Based on the slope of the v^2 vs. T plot for $T<T_C$, together with the value of d calculated earlier, we may now compute the thickness of the cooperatively-moving fluid. For the 24 nm nanoparticle at pH=5.10 and for the 106 nm nanoparticle at pH=5.20 in water, the thicknesses of the cooperatively-moving fluid are 1×10^{-6} m and 4×10^{-7} m, respectively. The values are different, but quite close considering that the calculation is heuristic. The calculation corroborates with our simulation observation that the size of the LDL motif grows rapidly at around T_C (Figure 3d of the manuscript). Additionally, we note that the luminescent thermal probes described in this work are hydrophilic ligand-free Ln^{3+}-doped upconverting nanoparticles that are stabilized in aqueous suspensions by electrostatic interactions. There is a double layer structure formed on the nanoparticle surface, which can be quantified by measurements of the zeta potential. Because of the electrostatic interactions, a layer of water "sticks" to the nanoparticle surface. This layer of water should be considered as part of the nanoparticle probe. As a result, what the bulk water see is a nanoparticle with a surface layer of water and the property of the bulk water is not strongly disturbed by the probe. Therefore, it is reasonable that the thickness of the cooperatively-moving fluid is much larger than the size of the bare nanoparticles.

We note that the hydrodynamic effects in this section concern the momentum and mass transport of the fluid surrounding the nanoparticles. The regime of the liquid motion influences the Brownian velocity of the nanoparticles, but should not be confused with the regime of transport of the nanoparticles. The vortex shell that is only formed in the immediate vicinity of the nanoparticles, but not in the entire nanofluid.

S2.3 Instantaneous Brownian velocity and thermal diffusivity

The diffusion of particles with at least one dimension lower than 1000 nm is treated as Brownian motion. There is no principal distinction between diffusion and Brownian motion since both denote the same thermal motion[19]. Specifically, Brownian motion at different time scales is defined relative to the linear momentum relaxation time (τ_M, defined as the time needed for the momentum to relax to 1/e of its initial value). Brownian motion is called ballistic (in the limit $t \ll \tau_M$) or diffusive (in the limit $t \gg \tau_M$). Typical values of τ_M are ~0.1 ns for nanoparticles of 25 nm in diameter.

Different from the methods based on analysis of the Brownian motion of a single microparticle confined by a harmonic optical trap[20], the method described here determines the changes in temperature by mapping luminescence profiles of the nanocrystals suspended in a container.

The velocity obtained in this work corresponds to the instantaneous Brownian velocity of the nanoparticles, as discussed in 2016[1]. Briefly, the increase in temperature increases the instantaneous Brownian velocity of the nanoparticles through nanoconvection at a timescale $\tau_S \sim 10^{-12}$ s (the time required for a sound wave with a velocity v_s to travel a distance equivalent to the radius a of the nanoparticle).

During the momentum relaxation time, the nanoparticles are in thermal equilibrium with the solvent molecules, giving rise to changes in each particle's instantaneous Brownian velocity. In other words, as $\tau_S/\tau_M \sim 10^{-2}$, the thermalization occurs in a time period 100 times shorter than the momentum relaxation, the temperature changes occur before the nanoparticles enter the diffusive regime. In this sense, we denote the rate of temperature change in the nanofluid container as the instantaneous Brownian velocity of the nanoparticles.

The linearity obtained between the thermal diffusivity of the nanofluid α and the instantaneous Brownian velocity v of the nanoparticles in the dilute nanofluids (**Figure S16D**, **Figure S17D,** and **Figure S18D**) validates the measurement of Brownian velocity through upconversion thermometry. In fact, as the thermal diffusivity is defined as:

$$\alpha = \frac{\kappa}{\rho c_p} \qquad \textbf{(S14)}$$

where κ is the thermal conductivity, ρ the specific mass and c_p the specific heat of the nanofluid, the linearity between α and v imply that the velocity of the nanoparticles must also be linear to κ. This observation is in agreement with the model postulated by Kumar *et al.*[21]:

$$\kappa = \frac{1}{3} NLc_p \frac{\phi\, r_s}{(1-\phi)a}\ v + k_F \qquad \textbf{(S15)}$$

where *N* is the mean number of nanoparticles per unit of volume, *L* is the mean free path of the nanoparticle, v is the average particle velocity (corresponding to the Brownian velocity either in the diffusive or in the ballistic regime), k_F is the thermal conductivity of the base fluid and r_s is the radius of the solvent molecule.

S3 Supplementary Figures
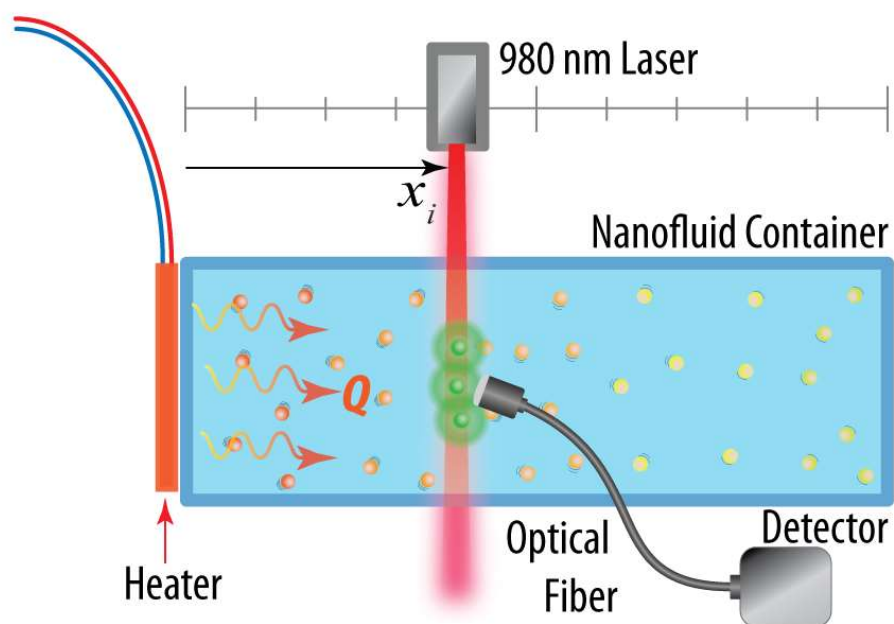
Figure S1. Schematic of the measurement set-up used to record the temperature profiles of the nanofluids. The laser diode is positioned on a precisely controlled moving stage, allowing the nanofluid to be irradiated at different locations along the predesigned path of the heat flux Q (*xx* direction). Subsequently, a collimating lens collects the upconversion emission, and the optical signal is guided to a fiber-coupled detector.
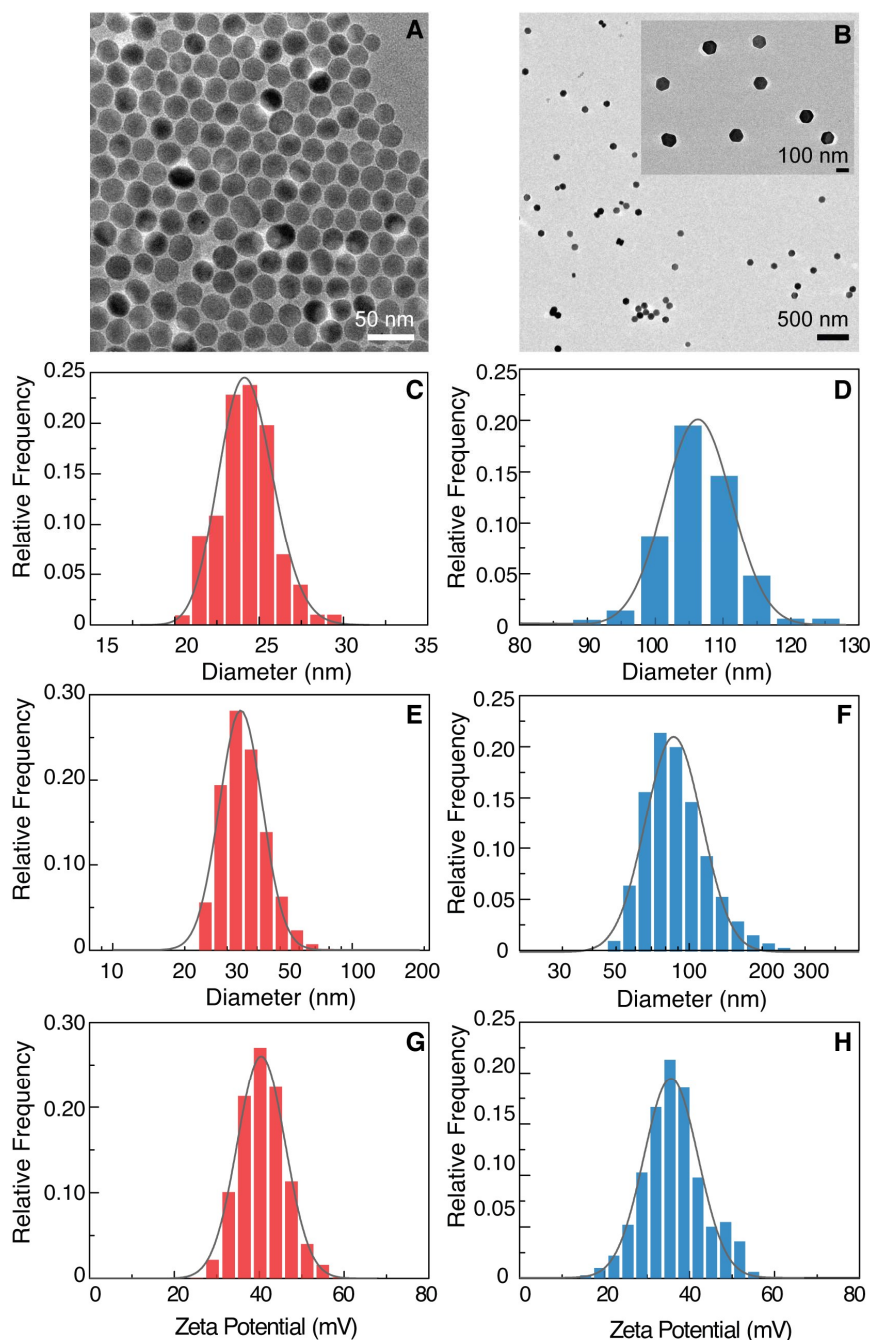
Figure S2. Particle size and zeta potential of the nanocrystals. (**A**) and (**B**) TEM images of NaYF$_4$:Yb/Er@NaYF$_4$ and NaYF$_4$:Lu/Yb/Er, respectively. (**C**) and (**D**) TEM size distribution of NaYF$_4$:Yb/Er@NaYF$_4$ and NaYF$_4$:Lu/Yb/Er, respectively. (**E**) and (**F**) Hydrodynamic size distribution of NaYF$_4$:Yb/Er@NaYF$_4$ and NaYF$_4$:Lu/Yb/Er nanoparticles, in distilled water, pH=5.10±0.01 and pH=5.20±0.01, respectively. (**G**) and (**H**) Zeta potential of NaYF$_4$:Yb/Er@NaYF$_4$ and NaYF$_4$:Lu/Yb/Er in distilled water at the same pH values, respectively. The lines are the best fits for the hydrodynamic and TEM size data (log-normal distribution) and zeta potential (Gaussian distribution). The summary of the fitting results is presented in **Table S2**.
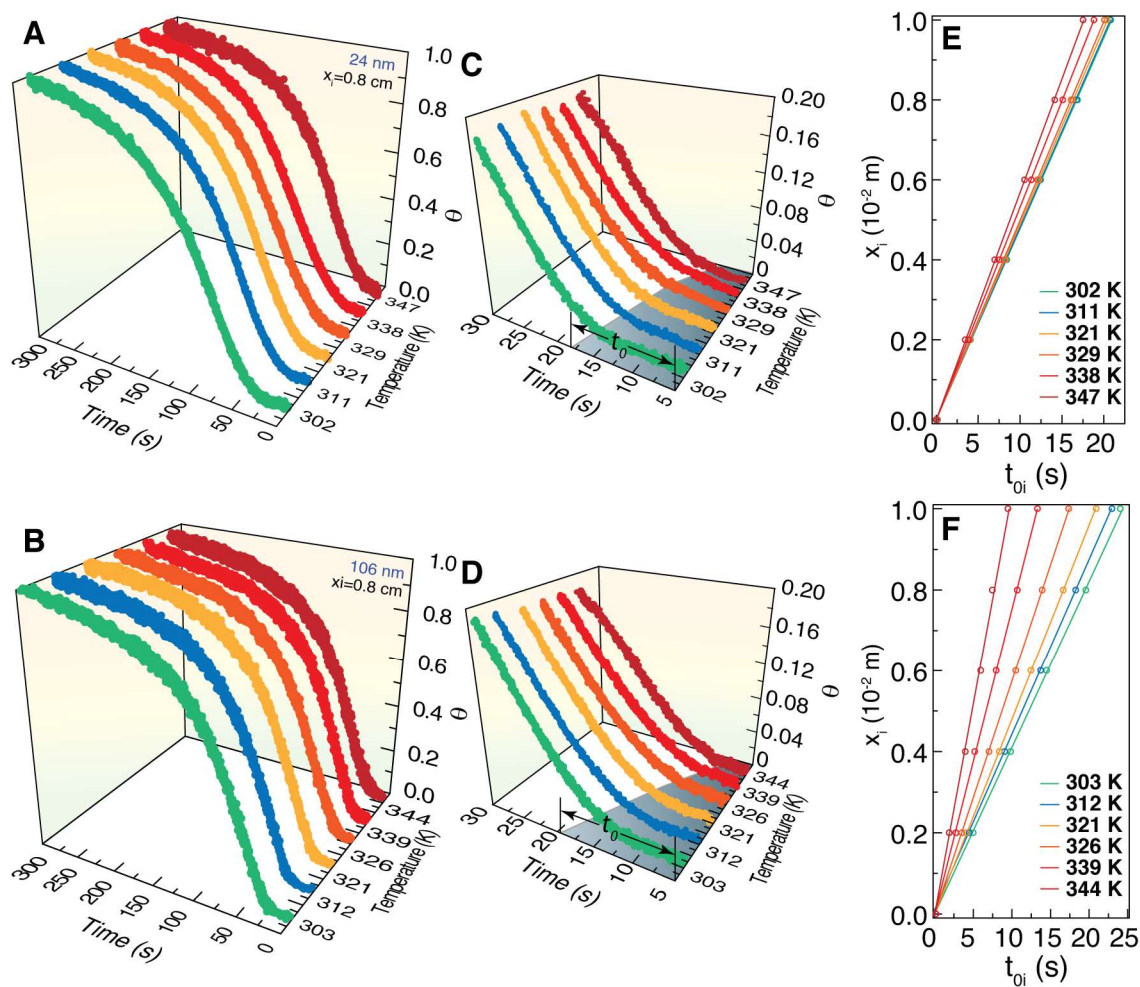
Figure S3. The time-dependent temperature profile of the water-based NaYF₄:Yb/Er@NaYF₄ and NaYF₄:Lu/Yb/Er nanofluids. Keeping the distance to the heating plane fixed at $x_i=0.8\times10^{-2}$ m the reduced temperature profiles of the 24 nm (**A**) and 106 nm (**B**) nanoparticles dispersed in water (pH=5.10±0.01 and 5.20±0.01, respectively) are recorded with respect to the elapsed time for distinct initial temperature values of the nanofluids. Similar results are obtained for distinct x_i positions. (**C**) and (**D**) Magnification of the first 30 seconds of the time-dependent profiles of the 24 nm and 106 nm nanoparticles, respectively. The shadowed area marks the critical time t_{0i} when the onset of the change in the intensity ratio is observed due to temperature variation upon turning on the heater. The critical time t_{0i} of the 24 nm and 106 nm nanoparticles depends on the nanofluids' initial temperature. (**E**) and (**F**) The corresponding linear correlation ($r^2 >0.994$) between x_i and t_{0i} for different nanofluids' temperatures.
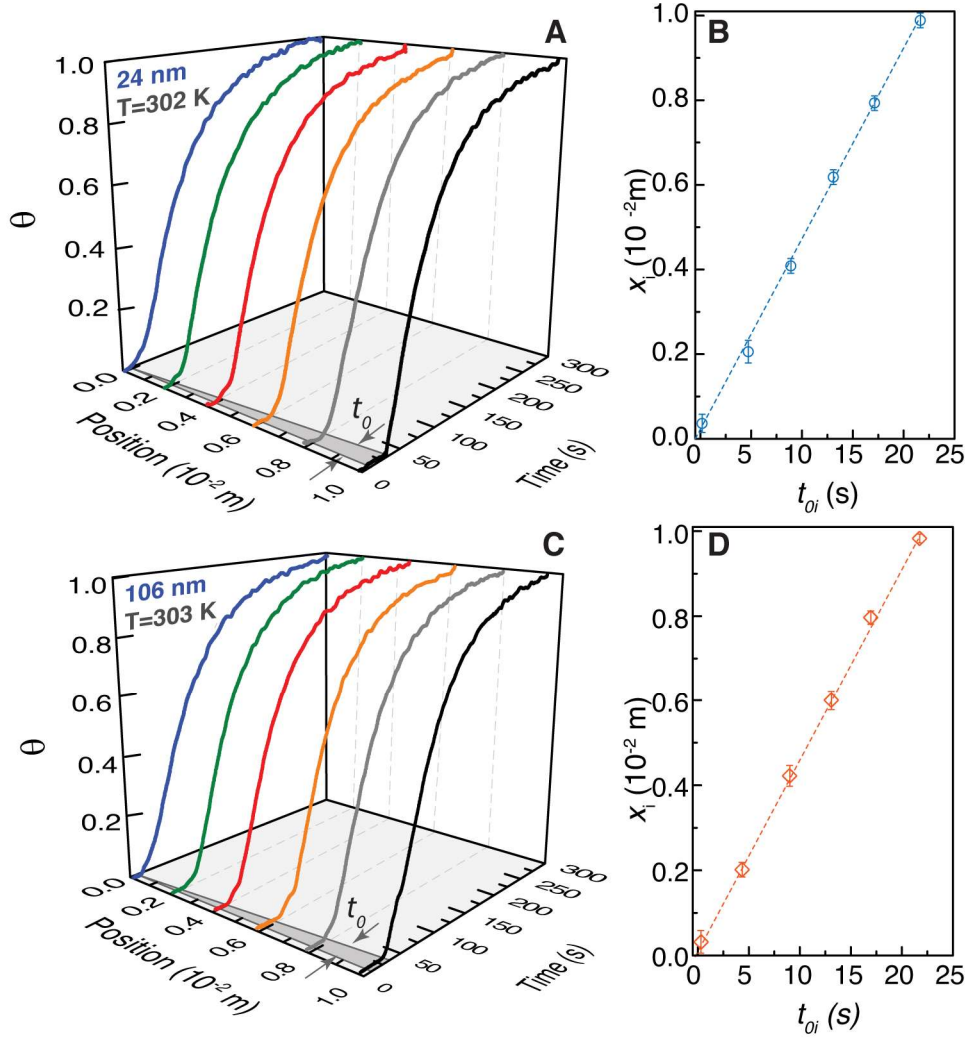
Figure S4. The time-dependent temperature profile of the water-based NaYF₄:Yb/Er@NaYF₄ and NaYF₄:Lu/Yb/Er nanofluids. (**A**) and (**B**) Reduced temperature profile of the 24 nm and 106 nm nanoparticles dispersed in water (ϕ=0.085% and 0.066%, respectively) at an initial temperature of 302 K and pH=5.10±0.01 (smaller particles) and 303 K and 5.20±0.01 (bigger particles), as measured when the laser excitation is positioned at different distances to the heating plane, x_i, along the xx direction (Q=4.63×10⁴ W·m⁻²). The shadowed area marks the critical time t_{0i} when the onset of the change in the intensity ratio is observed due to temperature variation upon turning on the heater. (**C**) and (**D**) The corresponding linear correlation (r^2 >0.994) between x_i and t_{0i}.
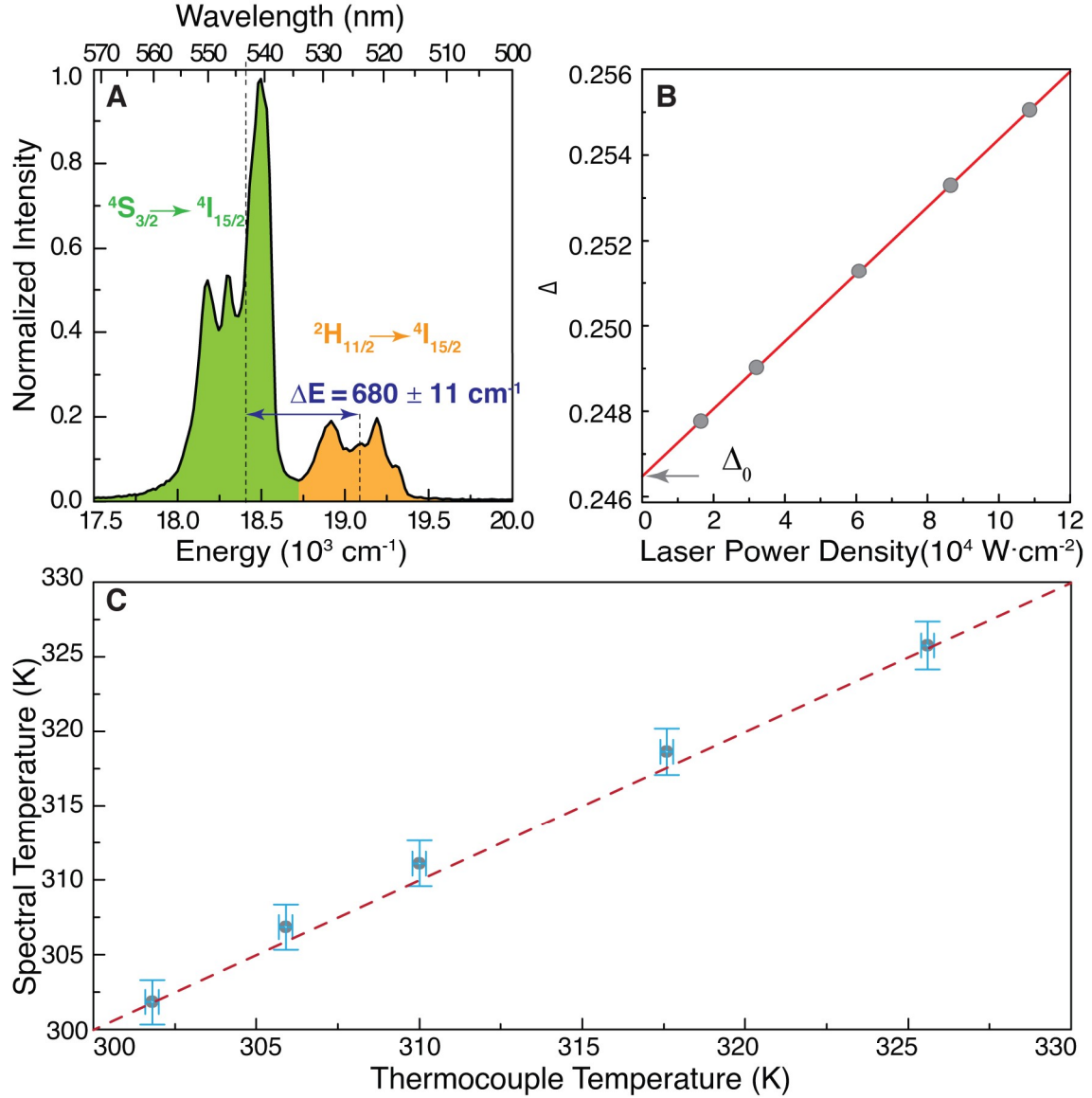
Figure S5. Calibration curve of NaYF$_4$:Yb/Er(18/2%)@NaYF$_4$. (**A**) Barycenters of the $^2H_{11/2}{\rightarrow}^4I_{15/2}$ and $^4S_{3/2}{\rightarrow}^4I_{15/2}$ transitions in the emission spectrum of the water suspension of 24 nm nanoparticles at 300 K. (**B**) Dependence of the parameter Δ on the laser power density. The solid line is the best fit of experimental data to a straight line ($r^2 > 0.999$) and allows for the determination of Δ_0=0.2465 as the intercept corresponding to T_0=300 K. (**C**) Temperature computed from Eq. 3 of the manuscript (spectral temperature, y) *versus* temperature reading from the immersed thermocouple (thermocouple temperature, x). The straight line is a guide for the eyes and corresponds to $y=x$. The agreement between the spectral and thermocouple temperatures is excellent. The horizontal and vertical error bars stand for the experimental temperature uncertainty and the error in the determination of spectral temperature based on the ΔE and Δ_0 values, respectively.

Figure S6. Calibration curve of NaYF₄:Lu/Yb/Er (50/18/2%). (**A**) Barycenters of the $^2H_{11/2}{\rightarrow}^4I_{15/2}$ and $^4S_{3/2}{\rightarrow}^4I_{15/2}$ transitions in the emission spectrum of the water suspension of 106 nm nanoparticles at 300 K. (**B**) Dependence of the parameter $\varDelta$ on the laser power density. The solid line is the best fit of experimental data to a straight line ($r^2 > 0.999$) and allows for the determination of $\varDelta_0$=0.2431 as the intercept corresponding to T_0=295 K. (**C**) Temperature computed from Eq. 3 of the manuscript (spectral temperature, y) *versus* temperature reading from the immersed thermocouple (thermocouple temperature, x). The straight line is a guide for the eyes and corresponds to $y=x$. The agreement between the spectral and thermocouple temperatures is excellent. The horizontal and vertical error bars stand for the experimental temperature uncertainty and the error in the determination of spectral temperature based on the ΔE and $\varDelta_0$ values, respectively.
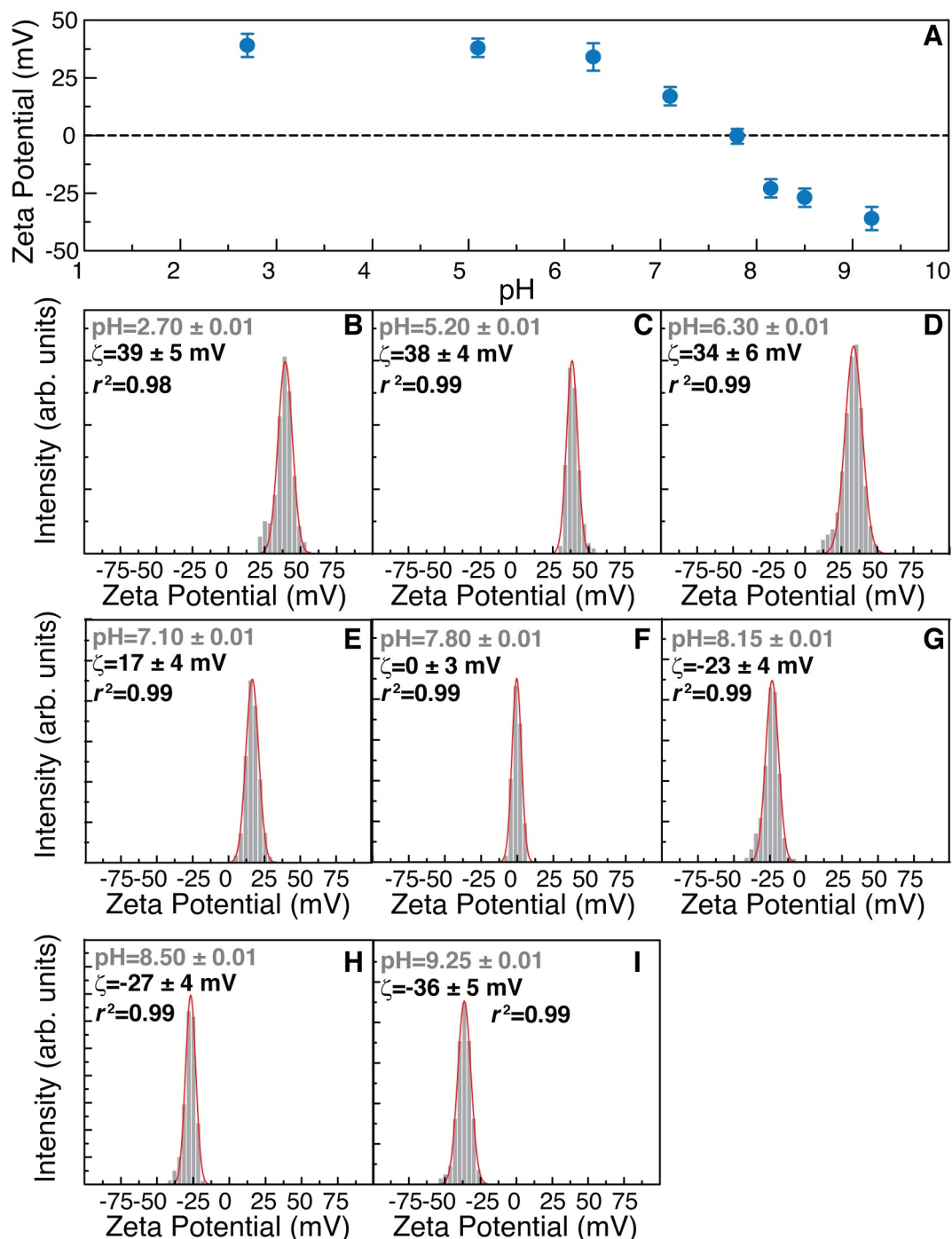
Figure S7. pH dependence of the Zeta potential. (**A**) pH dependence of the Zeta potential of the 106 nm nanoparticles in water. (**B-I**) Corresponding histograms of the Zeta potential for each pH value. The lines are the best fits to the data potential using Gaussian distributions.
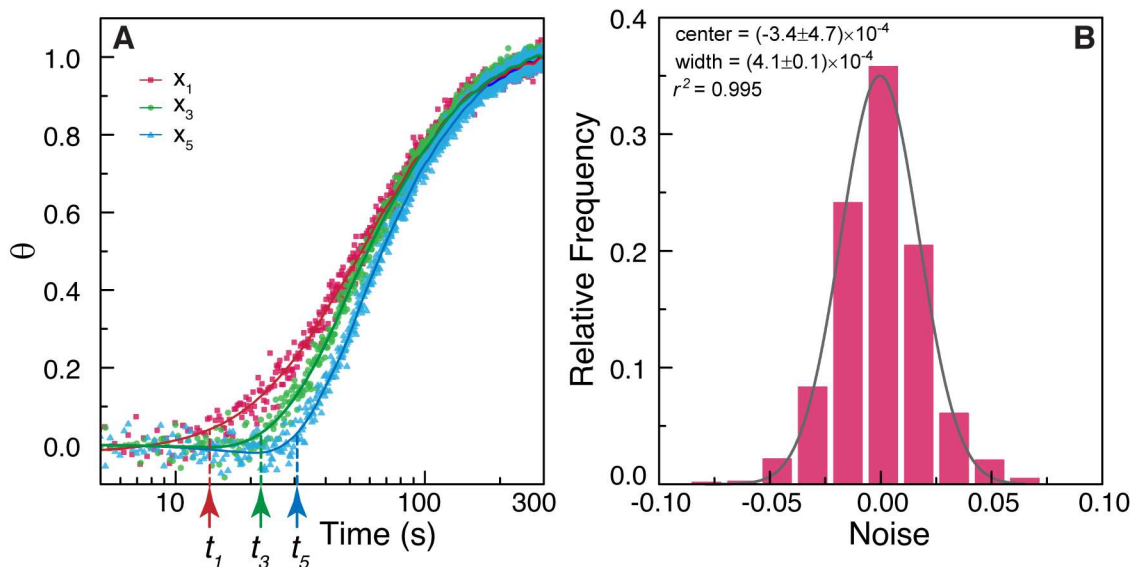
Figure S8. White Gaussian noise. (**A**) Illustrative denoising procedure applied to three reduced temperature curves (symbols) of the 24 nm nanoparticles in water (pH=5.10±0.01, Q=4.63×10^4 W·m^{-2}) acquired at x_1=0.05 cm, x_3=0.40 cm, and x_5=0.80 cm. The solid lines correspond to the denoised data using the DWT method and the corresponding t_{0i} values are indicated. (**B**) Noise histogram (10 classes) calculated for an illustrative experimental curve. The lines are fits to the experimental data using Gaussian functions. Considering the high correlation coefficients, the noise is called white Gaussian noise.
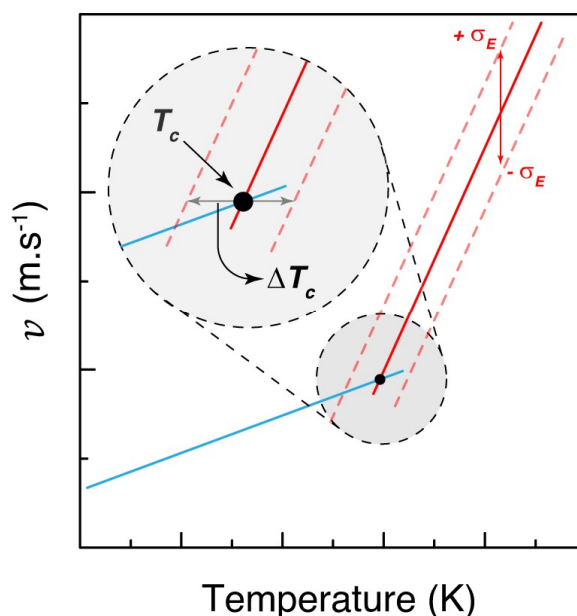
Figure S9. Schematic representation of the calculation of $T_c \pm \Delta T_c$. The solid lines are the best fits to the instantaneous Brownian velocity data below (blue) and above (red) T_c. The dashed lines display the standard error of the estimate for the $T > T_c$ regime.
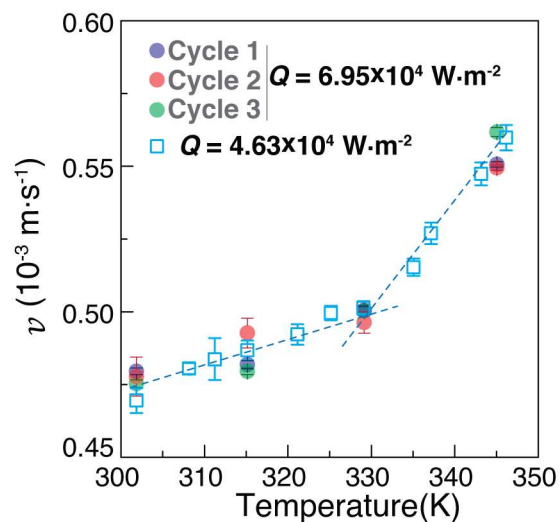
Figure S10. Temperature cycling. Instantaneous Brownian velocity of the 24 nm nanoparticles in water (pH=5.10±0.01) measured during three consecutive heating cycles between 303 and 343 K at Q=6.95×10^4 W·m^{-2}. Values obtained in a different day at Q=4.63×10^4 W·m^{-2} are also depicted. The lines are guides for the eyes.
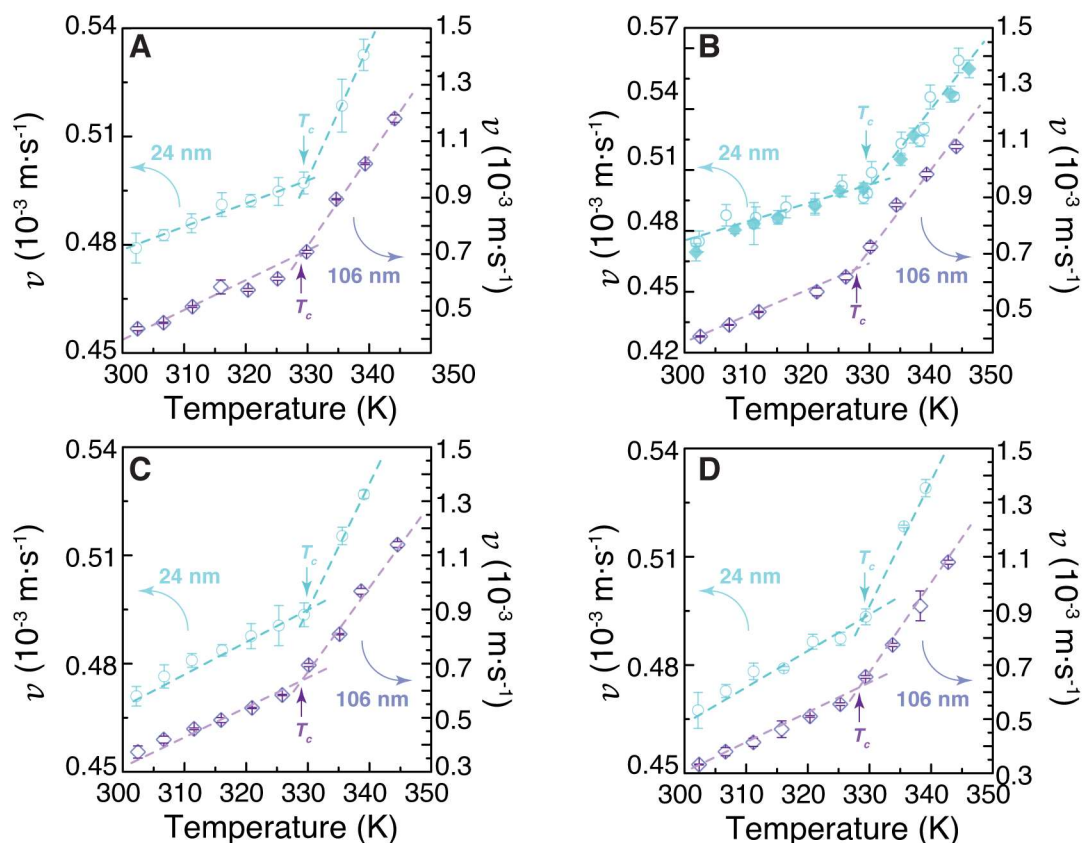
Figure S11. Comparison of the temperature dependence of the instantaneous Brownian velocity for different sized nanocrystals. Temperature-dependent instantaneous Brownian velocities of the 24 nm (circles) and 106 nm (diamonds) nanoparticles suspended in water heated at 4.63×10^4 W m^{-2} at distinct pH values, (**A**) 2.70±0.01, (**B**) 5.10±0.01 (24 nm), and 5.20±0.01 (106 nm), (**C**) 6.40±0.01 and (**D**) 8.50±0.01. The lines are the best fits to straight lines (slopes and correlation coefficients r^2 shown in Table S3).
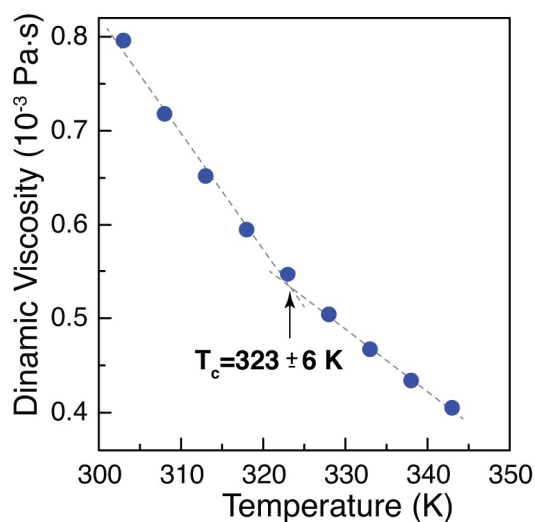
Figure S12. Bi-linear behaviour of the dynamic water viscosity with temperature. The points were extracted from Ref. 19 whereas the dashed lines are the best fits to straight lines with slopes $-(1.24\pm0.06)\times10^{-5}$ Pa·s·K^{-1} and $-(0.66\pm0.02)\times10^{-5}$ Pa·s·K^{-1} ($r^2>0.988$).
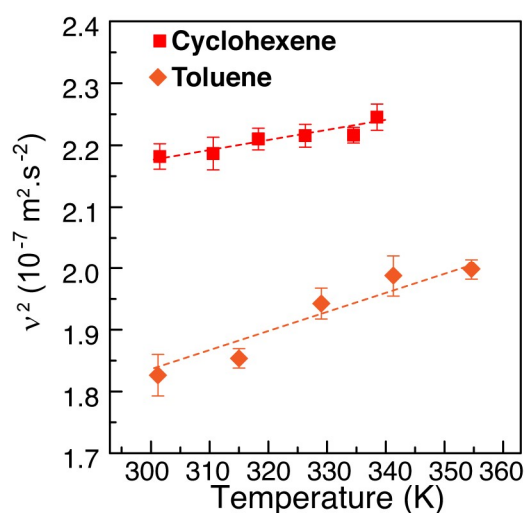

Figure S13. Temperature-dependent v^2 values in toluene and cyclohexene. Temperature-dependent v^2 values of the 24 nm nanoparticles in toluene and cyclohexene (Q=6.95×10^4 W·m^{-2}). The lines are the best fits to straight lines (the slopes and correlation coefficients r^2 are presented in Table S4).

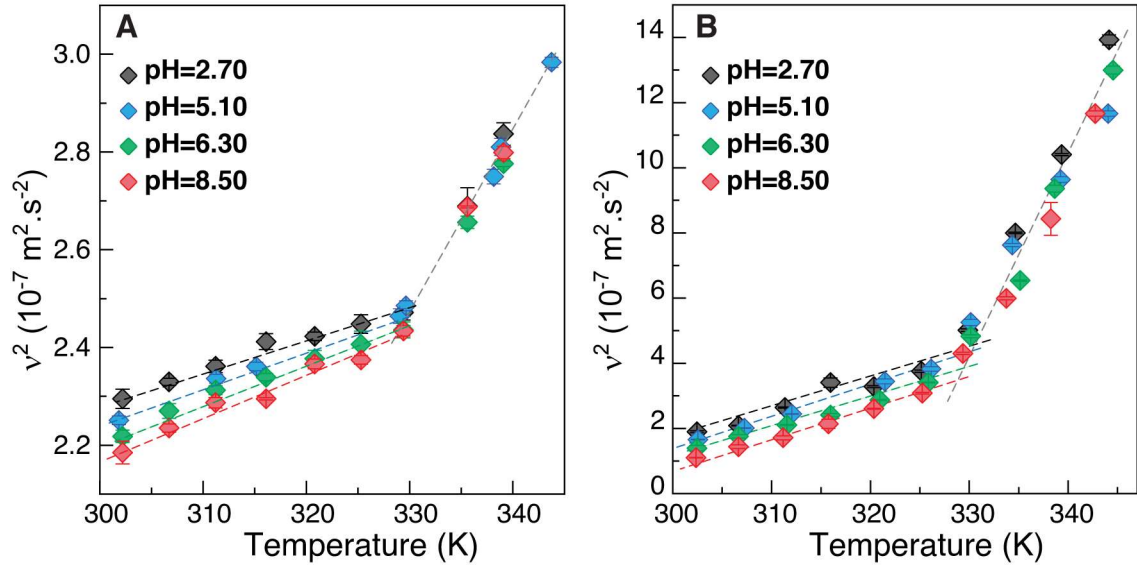**Figure S14. Temperature-dependent v^2 values in water.** Temperature-dependent v^2 values of the (**A**) 24 nm and (**B**) 106 nm nanoparticles in the water at distinct pH values (Q=6.95×10^4 W·m^{-2}). The lines are the best fits to straight lines (the slopes and correlation coefficients r^2 are presented in Table S4).
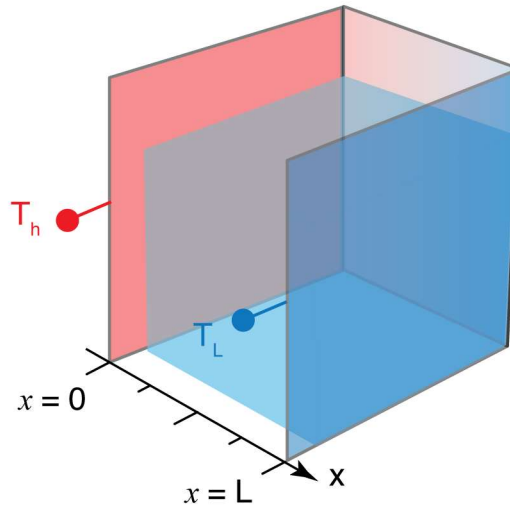

Figure S15. Modeling of heat transport for pure water. The two-plate model used to mimic the thermal transport occurring in the water-based nanofluids. The total transport length is assumed to be 1 cm, as in the experiment.
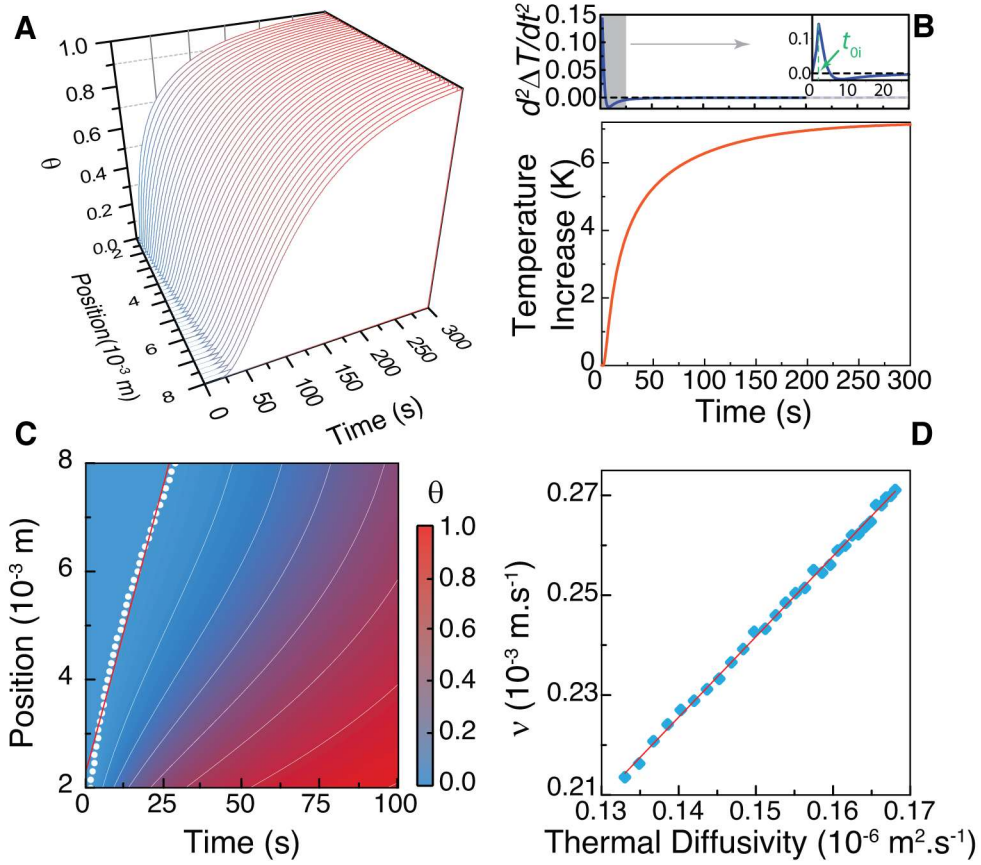
Figure S16. Results from two plate model for T_0-T_L=9 K. (**A**) Three-dimensional plot of normalized temperature as a function of time and position. (**B**) Temperature as a function of time at position x_i=0.2 cm. The time instant corresponding to the maximum of the temperature's second derivative is t_{0i}. (**C**) Zoomed-in contour plot of the first 100 seconds of panel B. The points are the maximum position of the second derivative, and the line is the linear fit, which gives the instantaneous Brownian velocity. (**D**) Instantaneous Brownian velocity versus thermal diffusivity of pure water over the temperature range 273-373 K. The line is the linear fit used to obtain the predicted thermal diffusivity of the nanoparticle-water mixture.

Figure S17. Results from two plate model for T_0-T_L=21 K. (A) Three-dimensional plot of normalized temperature as a function of time and position. (**B**) Temperature as a function of time at position x_i=0.2 cm. The time instant corresponding to the maximum of the temperature's second derivative is t_{0i}. (**C**) Zoomed-in contour plot of the first 100 seconds of panel B. The points are the maximum position of the second derivative, and the line is the linear fit, which gives the instantaneous Brownian velocity. (**D**) Instantaneous Brownian velocity versus thermal diffusivity of pure water over the temperature range 273-373 K. The line is the linear fit used to obtain the predicted thermal diffusivity of the nanoparticle-water mixture.
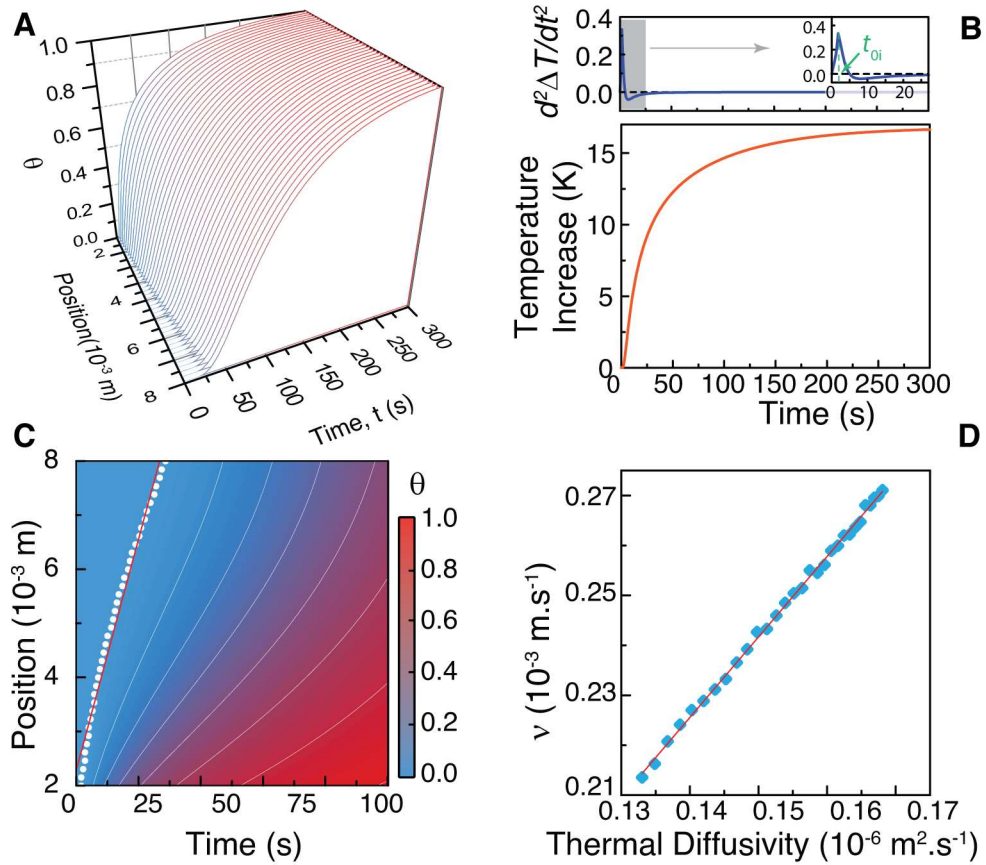
Figure S18. Results from two plate model for T_0-T_L=25 K. (**A**) Three-dimensional plot of normalized temperature as a function of time and position. (**B**) Temperature as a function of time at position x_i=0.2 cm. The time instant corresponding to the maximum of the temperature's second derivative corresponds is t_{0i}. (**C**) Zoomed-in contour plot of the first 100 seconds of panel B. The points are the maximum position of the second derivative, and the line is the linear fit, which gives the instantaneous Brownian velocity. (**D**) Instantaneous Brownian velocity versus thermal diffusivity of pure water over the temperature range 273-373 K. The line is the linear fit used to obtain the predicted thermal diffusivity of the nanoparticle-water mixture.
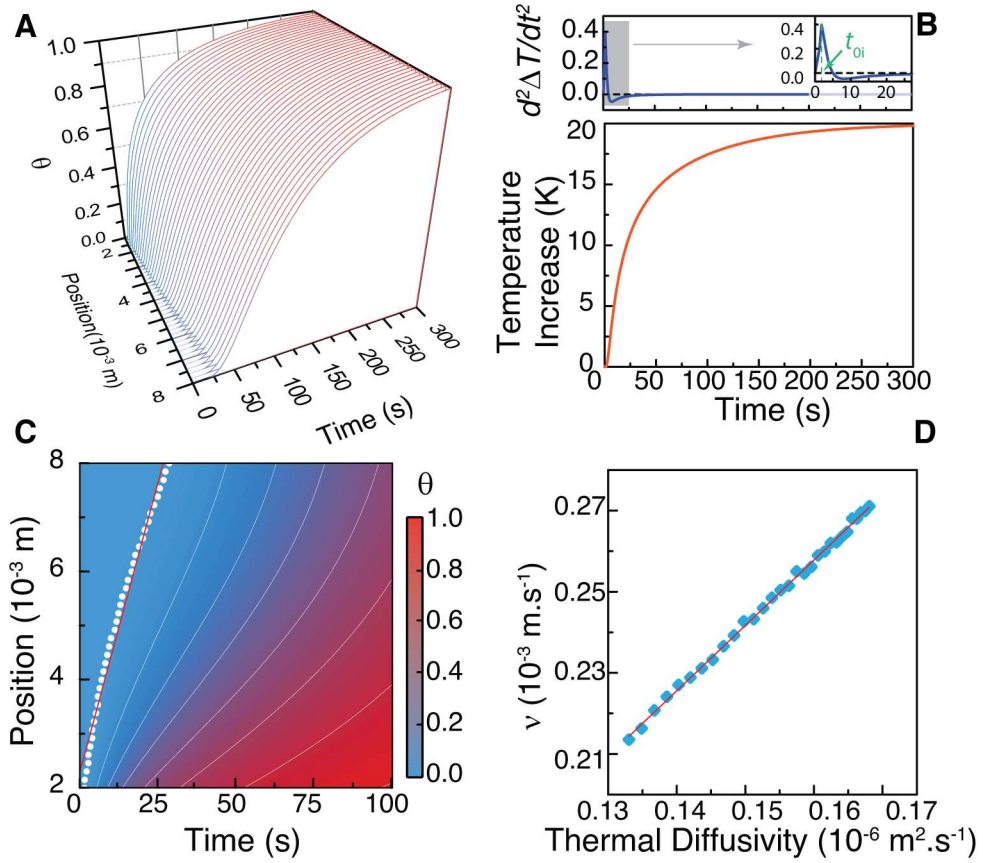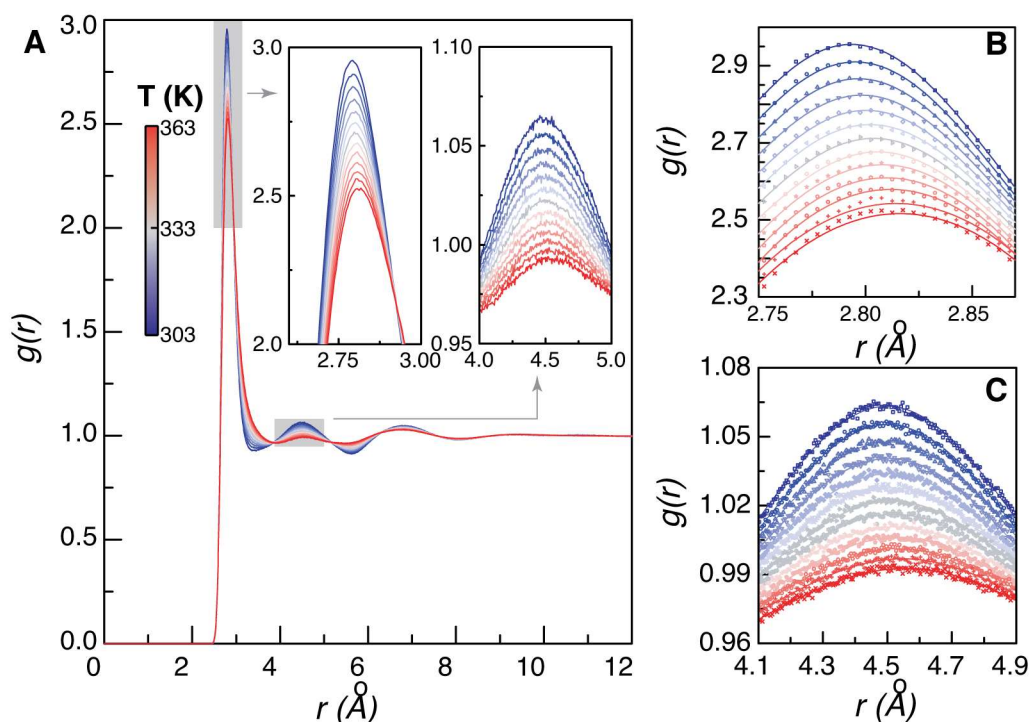
Figure S19. O-O radial pair distribution function and the location of the 1st and the 2nd peak maxima, r_1 and r_2. (**A**) O-O radial distribution function, $g(r)$, computed from a simulation of 1024 water molecules. (**B**) $g(r)$ in the vicinity of r_1. Least-square fit by a Gaussian function is shown as black curves. (**C**) $g(r)$ in the vicinity of r_2. Least-square fit by Gaussian function is shown as solid curves.
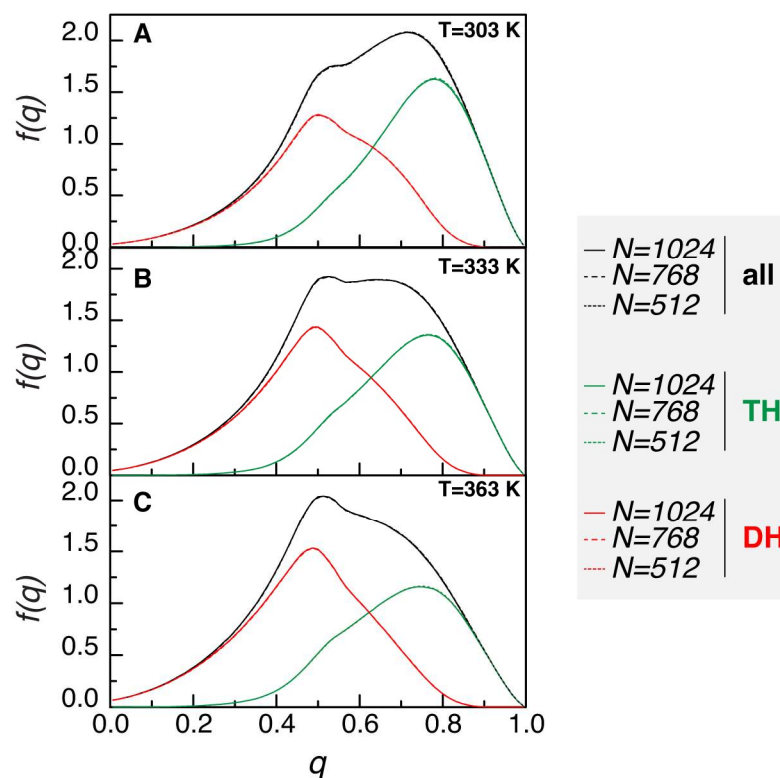
Figure S20. Finite-size effect of the simulation for the probability density function _f(q)_. The three panels represent the probability density function _f(q)_ of the orientational order parameter _q_ (Eq.1 in the main text) for water at (**A**) 303 K, (**B**) 333 K, and (**C**) 363 K, respectively. In each panel, data is calculated based on the molecular dynamics simulation of a cubic box of N=512, 768, and 1024 water molecules with the polarizable SWM4-NDP water model. The finite-size effect of the simulation is minimal.

Figure S21. Finite-size effect of the simulation for the statistics of molecular structures. (**A**) The probability x_{TH} for a water molecule to be in the TH-state as a function of temperature from data based on the molecular dynamics simulation of a cubic box of N=512, 768, and 1024 water molecules with the polarizable SWM4-NDP water model. The finite-size effect of the simulation is minimal. (**B**) The probability for the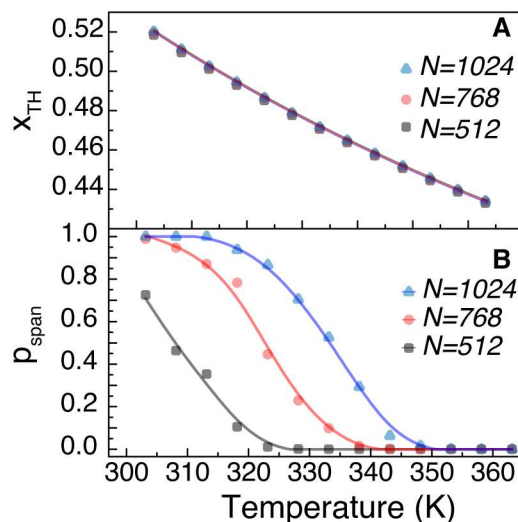 LDL motif to span across a 24 nm nanoparticle based on Eq. S11. Since N=1024 is the largest simulation box considered, it gives the best estimate for the probability p_{span}. All simulations indicate a crossover from 1 to 0 at around T=330 K.
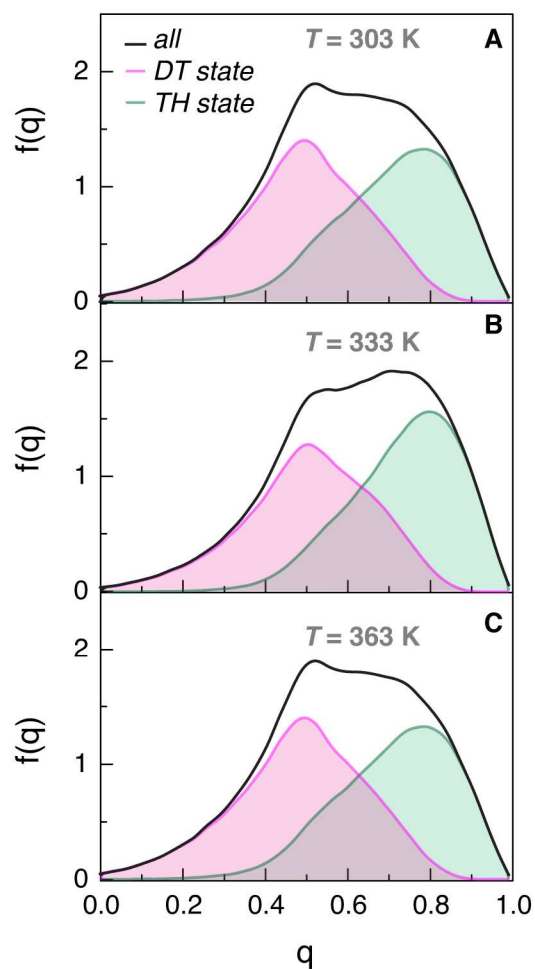
Figure S21. Probability density functions based on simulations using TIP4P-FB model. The probability density function *f(q)* of the orientational order parameter *q* (Eq. 1 in the manuscript) for water at **A** 303 K, **B** 333 K, and **C** 363 K, calculated based on the molecular dynamics simulation of a cubic box of 1024 water molecules with the nonpolarizable TIP4P-FB water model. The contributions towards *f(q)* of the locally tetrahedral (TH) state and the locally disturbed (DT) state are shown as shaded areas.

Figure S22. Fraction of molecules in the TH-state computed with simulations using the TIP4P-FB and SWM4-NDP models. The fraction of molecules in the TH-state is denoted as x_{TH}.

S4 Supplementary Tables

Table S1. Mass concentration ρ_F (kg·m^{-3}) and volume fraction ϕ (%) of the NaYF$_4$:Yb/Er@NaYF$_4$ and NaYF$_4$:Lu/Yb/Er nanocrystals in water, cyclohexene and toluene.
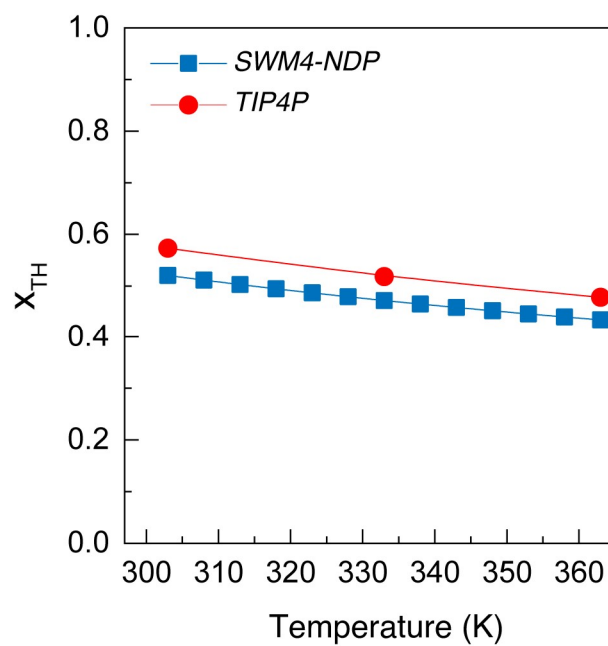
Solvent	Composition and size	ρ_F	ϕ
Water $\phi = \dfrac{\rho_F}{\rho_N}$	NaYF$_4$:Yb/Er(18/2%)@NaYF$_4$ (24 nm)	3.75	0.085
	NaYF$_4$:Lu/Yb/Er (50/18/2%) (106 nm)	3.75	0.066
Cyclohexene and toluene $\phi = \dfrac{\rho_{F(1-x)}}{\rho_N} + \dfrac{\rho_F x}{\rho_{OA}}$	NaYF$_4$:Yb/Er(18/2%)@NaYF$_4$ (24 nm)	3.75	0.107

ρ_N (24 nm)=4390 kg·m^{-3}; ρ_N (106 nm)=5680 kg·m^{-3} are the densities of the crystals
ρ_{OA}=890 kg·m^{-3} is the density of the oleic acid capping with mass fraction x=0.063.

Table S2. TEM and hydrodynamic diameters (nm), Zeta potential (mV) and pH of NaYF$_4$:Yb/Er@NaYF$_4$ and NaYF$_4$:Lu/Yb/Er. The hydrodynamic diameter, Zeta potential and pH are ascribed to water-based suspensions.

Suspension	TEM diameter	Hydrodynamic diameter	Zeta Potential	pH
NaYF$_4$:Yb/Er (18/2%)@NaYF$_4$	24.2±2.1	36±8	40±5	5.10±0.01
NaYF$_4$:Lu/Yb/Er (50/18/2%)	106.3±9.7	93±26	37±6	5.20±0.01

The data of TEM and hydrodynamic size results from the best fits to the distribution data using a log-normal function (r^2>0.998 for TEM fits and r^2>0.980 for the hydrodynamic ones), whereas that of the zeta potential results from the best fits to the distribution data using a Gaussian function (r^2>0.970). The errors correspond to ± fwhm of the corresponding fitting curves.

Table S3. Slopes (s, 10^{-6} m·s^{-1}·K^{-1}) and correlation coefficients of $\nu(T)$ in the water-, cyclohexene- and toluene-based nanofluids heated at $Q=4.63\times10^4$ W m^{-2}, and slopes (s, 10^{-7} m^2·s^{-1}·K^{-1}) and correlation coefficients of effective diffusivity for the nanofluid containing 24 nm nanoparticles.

Nanofluid	Temperature Range	pH	s	r²
NaYF₄:Yb/Er@NaYF₄ - *Brownian Velocity*				
Water	T<Tc	2.70±0.01	0.69±0.04	0.981
		5.10±0.01	1.08±0.12	0.917
		6.30±0.01	0.84±0.07	0.967
		8.50±0.01	0.81±0.13	0.881
	T>Tc	all values	3.37±0.15	0.976
Cyclohexene	302-339	-	0.57±0.03	0.986
Toluene	301-355	-	0.40±0.05	0.928
NaYF₄:Lu/Yb/Er - *Brownian Velocity*				
Water	T<Tc	2.70±0.01	8.35±0.68	0.968
		5.20±0.01	9.11±0.31	0.997
		6.30±0.01	8.73±0.24	0.996
		8.50±0.01	9.82±0.58	0.999
	T>Tc	all values	27.6±2.4	0.896
NaYF₄:Yb/Er@NaYF₄ - *Effective Diffusivity*				
Water	T<Tc	5.10±0.01	6.15±0.81	0.853
	T>Tc		28.3±1.2	0.993

Table S4. Slopes (s, 10^{-9} m^2·s^{-2}·K^{-1}) and correlation coefficients r^2 of the temperature dependence of ν^2 values in the water, cyclohexene- and toluene-based nanofluids at $Q=4.63\times10^4$ W m^{-2}.

Nanofluid	Temperature Range	pH	s	r^2
NaYF$_4$:Yb/Er@NaYF$_4$				
Water	$T<T_c$	2.70±0.01	0.67±0.04	0.98
		5.10±0.01	1.01±0.07	0.93
		6.30±0.01	0.81±0.06	0.97
		8.50±0.01	0.77±0.12	0.88
	$T>T_c$	all values	3.49±0.15	0.98
Cyclohexene	302-339	-	0.54±0.02	0.99
Toluene	301-355	-	0.36±0.04	0.93
NaYF$_4$:Lu/Yb/Er				
Water	$T<T_c$	2.70±0.01	8.79±0.67	0.97
		5.20±0.01	8.25±0.40	0.99
		6.30±0.01	8.87±0.40	0.99
		8.50±0.01	8.44±0.12	0.99
	$T>T_c$	all values	45.57±4.3	0.88

Table S5. Temperature (K) dependence of the density of water (ρ_L, 10^3 kg·m^{-3}) that determines the density of water molecules in molecular dynamics simulations.

Temperature	ρ_L
303	0.99565
308	0.99403
313	0.99221
318	0.99022
323	0.98804
328	0.98570
333	0.98321
338	0.98056
343	0.97778
348	0.97486
353	0.97180
358	0.96862
363	0.96531

Table S6. Slopes (s, 10^{-4} Å·K^{-1}) and correlation coefficients of $r_1(T)$ and $r_2(T)$ in water.

Method	g(r) peak	Temperature Range	s	r²
Simulation of SWM4-NDP	r_1	--	3.80±0.06	0.997
	r_2	$T<T_c$	4.35±0.45	0.960
		$T>T_c$	13.5±0.6	0.988
Experiment by Skinner et. al. [16]	r_1	--	3.08±0.19	0.920
	r_2	$T<T_c$	5.42±0.10	0.639
		$T>T_c$	36.3±5.22	0.923

S5 References

1. Brites C. D._, et al._ Instantaneous ballistic velocity of suspended brownian nanocrystals measured by upconversion nanothermometry. _Nat. Nanotechnol._ **11**, 851-856 (2016).
2. Bhattacharjee S. DLS and zeta potential - What they are and what they are not? _J. Control Release_ **235**, 337-351 (2016).
3. Bogdan N., Vetrone F., Ozin G. A. & Capobianco J. A. Synthesis of Ligand-Free Colloidally Stable Water Dispersible Brightly Luminescent Lanthanide-Doped Upconverting Nanoparticles. _Nano Lett._ **11**, 835-840 (2011).
4. Lang M., Guo H., Odegard J. E., Burrus C. S. & Wells R. O. Nonlinear processing of a shift-invariant discrete wavelet transform (DWT) for noise reduction. In: Wavelet Applications II; Szu HH, editor. Proc. SPIE 2491; 1995.
5. Donoho D. L. & Johnstone I. M. Ideal spatial adaptation by wavelet shrinkage. _Biometrika_ **81**, 425-455 (1994).
6. Donoho D. L. De-noising by soft-thresholding. _IEEE T. Inform. Theory_ **41**, 613-627 (1995).
7. Hellums J. D. & Churchill S. W. Transient and steady state, free and natural convection, numerical solutions: Part I. The isothermal, vertical plate. _AIChE J._ **8**, 690-692 (1962).
8. Carslaw H. S. & Jaeger J. C. _Conduction of Heat in Solids_, 2 edn. Oxford University Press: Oxford, U.K., 1986.
9. _Recommended Reference Materials for the Realization of Physicochemical Properties_. Blackwell Scientific Publications: Oxford, U.K., 1987.
10. Ramires M. L. V._, et al._ Standard Reference Data for the Thermal Conductivity of Water. _J. Phys. Chem. Ref. Data_ **24**, 1377-1381 (1995).
11. Sengers J. V. & Watson J. T. R. Improved International Formulations for the Viscosity and Thermal Conductivity of Water Substance. _J. Phys. Chem. Ref. Data_ **15**, 1291-1314 (1986).
12. Lamoureux G., Harder E., Vorobyov I. V., Roux B. & MacKerell Jr. A. D. A polarizable model of water for molecular dynamics simulations of biomolecules. _Chem. Phys. Lett._ **418**, 245-249 (2006).
13. Jiang W._, et al._ High-Performance Scalable Molecular Dynamics Simulations of a Polarizable Force Field Based on Classical Drude Oscillators in NAMD. _J. Phys. Chem. Lett._ **2**, 87-92 (2011).
14. Eastman P._, et al._ OpenMM 4: A Reusable, Extensible, Hardware Independent Library for High Performance Molecular Simulation. _J. Chem. Theory Comput._ **9**, 461-469 (2013).
15. McGibbon R. T._, et al._ MDTraj: A Modern Open Library for the Analysis of Molecular Dynamics Trajectories. _Biophys. J._ **109**, 1528-1532 (2015).
16. Skinner L. B., Benmore C. J., Neuefeind J. C. & Parise J. B. The structure of water around the compressibility minimum. _J. Chem. Phys._ **141**, 214507 (2014).
17. Chau P.-L. & Hardwick A. J. A new order parameter for tetrahedral configurations. _Mol. Phys._ **93**, 511-518 (1998).
18. Wang L.-P., Martinez T. J. & Pande V. S. Building Force Fields: An Automatic, Systematic, and Reproducible Approach. _J. Phys. Chem. Lett._ **5**, 1885-1891 (2014).
19. Bian X., Kim C. & Karniadakis G. E. 111 years of Brownian motion. _Soft Matter_ **12**, 6331-6346 (2016).
20. Huang R. X._, et al._ Direct observation of the full transition from ballistic to diffusive Brownian motion in a liquid. _Nat. Phys._ **7**, 576-580 (2011).
21. Kumar D. H._, et al._ Model for heat conduction in nanofluids. _Phys. Rev. Lett._ **93**, 144301-144304 (2004).